

# Integrated Open-Source Framework for Simulation of Transcatheter Pulmonary Valves in Native Right Ventricular Outflow Tracts

Christopher N. Zelonis<sup>1</sup>, Jalaj Maheshwari<sup>1\*</sup>, Wensi Wu<sup>1,2,3</sup>,  
Steve A. Maas<sup>4</sup>, Seda Aslan<sup>1</sup>, Kyle Sunderland<sup>5</sup>, Stephen Ching<sup>1</sup>,  
Ashley Koluda<sup>1</sup>, Yuval Barak-Corren<sup>1</sup>, Nicolas Mangine<sup>1</sup>, Patricia  
M. Sabin<sup>1</sup>, Andras Lasso<sup>5</sup>, Devin W. Laurence<sup>1,6</sup>, Christian Herz<sup>1</sup>,  
Matthew J. Gillespie<sup>6</sup>, Jeffrey A. Weiss<sup>4</sup>, Matthew A. Jolley<sup>1,6</sup>

<sup>1</sup>Department of Anesthesiology and Critical Care Medicine, Children's  
Hospital of Philadelphia, Philadelphia, 19104, PA, USA.

<sup>2</sup>Cardiovascular Institute, Children's Hospital of Philadelphia,  
Philadelphia, 19104, PA, USA.

<sup>3</sup>Department of Mechanical Engineering and Applied Mechanics,  
University of Pennsylvania, Philadelphia, 19104, PA, USA.

<sup>4</sup>Scientific Computing and Imaging Institute, University of Utah, Salt  
Lake City, 84112, UT, USA.

<sup>5</sup>Laboratory for Percutaneous Surgery, Queen's University, Kingston,  
K7L 2N8, ON, Canada.

<sup>6</sup>Division of Pediatric Cardiology, Children's Hospital of Philadelphia,  
Philadelphia, 19104, PA, USA.

\*Corresponding author(s). E-mail(s): [maheshwarj@chop.edu](mailto:maheshwarj@chop.edu);

## Abstract

**Background-** Pulmonary insufficiency is a consequence of transannular patch repair in Tetralogy of Fallot (ToF), leading to late morbidity and mortality. Transcatheter native outflow tract pulmonary valve replacement (TPVR) has become common, but assessment of patient candidacy and selection of the optimal device remains challenging. We demonstrate an integrated open-source workflow for simulation of TPVR in image-derived models to inform device selection.

**Methods-** Machine learning-based segmentation of CT scans was implemented to define the right ventricular outflow tract (RVOT). A custom workflow for

device positioning and pre-compression was implemented in SlicerHeart. Resulting geometries were exported to FEBio for simulation. Visualization of results and quantification were performed using custom metrics implemented in SlicerHeart and FEBio.

**Results-** RVOT model creation and device placement could be completed in under 1 minute. Virtual device placement using FE simulations visually mimicked actual device placement and allowed quantification of vessel strain, stress, and contact area. Regions of higher strain and stress were observed at the proximal and distal end locations of the TPVs where the devices impinge the RVOT wall. No other consistent trends were observed across simulations. The observed variability in mechanical metrics across RVOTS, stents, and locations in the RVOT highlights that no single device performs optimally in all anatomies, thereby reinforcing the need for simulation-based patient-specific assessment.

**Conclusions-** This study demonstrates the feasibility of a novel open-source workflow for the rapid simulation of TPVR which with further refinement may inform assessment of patient candidacy and optimal device selection.

**Keywords:** Congenital Heart Disease, Echocardiography, Valvular Heart Disease

## 1 Abbreviations

**2D** Two

**3D** Three Dimensional

**CHD** Congenital Heart Disease

**CTA** Computed Tomography Angiography

**DICOM** Digital Imaging and Communications in Medicine

**FE** Finite Element

**HGO** Holzapfel Gasser Ogden

**RVOT** Right Ventricular Outflow Tract

**RV-PA** Right Ventricle to Pulmonary Artery

**STL** Stereolithography

**ToF** Tetralogy of Fallot

**TPV** Transcatheter Pulmonary Valve

**TPVR** Transcatheter Pulmonary Valve Replacement

## 2 Introduction

Tetralogy of Fallot (ToF) is a form of congenital heart disease (CHD) characterized by pulmonary valve stenosis, right ventricular hypertrophy, a ventricular septal defect, and an overriding aorta. ToF is the most common form of cyanotic CHD, with a prevalence of about 5 out of every 10,000 live births [1]. In most cases of ToF, a surgical patch is placed to enlarge the pulmonary valve annulus (transannular patch). This patch relieves the obstruction to blood flow in infancy but results in loss of competence of the pulmonary valve. While initially tolerated, over time, severe regurgitation

of the pulmonary valve results in right ventricular dilation, ventricular failure, and life-threatening arrhythmias [2–5]. Surgical implantation of a bioprosthetic valve has been used to remedy pulmonary insufficiency and related complications, but has the associated morbidity of open heart surgery on cardiopulmonary bypass [6–10].

Over the last two decades, transcatheter pulmonary valve replacement (TPVR) has evolved to avoid the risks of open-heart surgery [9–11]. The first transcatheter pulmonary valve (TPV) devices available, the Melody valve (Medtronic, Minneapolis, MN) and Sapien valve (Edwards Lifesciences, Irvine, CA), were balloon-expandable bioprosthetic valves approved only for implantation in the small percentage of patients who received surgically placed cylindrical right ventricle-to-pulmonary artery (RV-PA) conduits as part of their initial repair [9, 10, 12]. However, the vast majority of patients with repaired ToF have surgically patched native outflow tracts, which demonstrate significant anatomic variability [13, 14]. As such, nearly 80% of patients with ToF are not candidates for traditional balloon expandable TPV therapies [7, 9–13, 15].

In order to meet this need, self-expanding TPV systems that can conform to a wide range of heterogeneous native RVOTs have been developed. In contrast to balloon-expandable TPVs, self-expanding TPVs consist of a spring-like Nitinol frame enclosing a tissue valve [16–18], which can expand to conform to the vessel and facilitate device retention. However, precise fit of the device in a given individual is critical; if the device is dislodged, it can catastrophically occlude the pulmonary outflow. Further, if the proximal and distal regions of the device do not effectively seal the pulmonary artery, a paravalvular leak or device thrombosis may result [16, 19, 20].

To date, the anatomical suitability of TPVR for a given patient is performed by the vendor using a screening CT scan of the RVOT [21]. For example, the screening process of the Harmony valve (Medtronic) was developed as part of the early feasibility study and subsequently refined during subsequent trials based on an engineering analysis that estimated degree of device oversizing (or interference) needed to secure the device in a given RVOT [16, 20, 22]. This analysis is now performed by measuring the circumference of the RVOT at different levels and overlaying the device shape on the perimeter-derived radius of the vessel, resulting in a “perimeter plot” [21]. However, this simplification of the anatomic geometry does not capture the true physical interaction of the device with the complex shape of the RVOT, and fails to account for vessel expansion in the setting of device placement [10]. In addition, many patients are not determined to be candidates for TPVR by standard criteria, but the sensitivity and specificity of these relatively simple screening processes are unknown [21]. As such, patients may be excluded unnecessarily due to conservative guidelines. Adding to the challenge, there are 3 different devices from two different manufacturers currently approved in the United States and over 15 different TPVs across a range of designs and sizes in use or in development internationally [16–18]. As the number of available devices for TPVR from a range of vendors increases, there is a growing need for an accurate method for assessing patient candidacy and matching the optimal device to an individual patient. In this setting, a more physically representative, patient-specific geometrical compatibility method to select the optimal device for an individual patient within a highly heterogeneous population is of increasing relevance.

In this study, we demonstrate the creation and initial application of an integrated workflow for the finite element (FE) simulation of self-expanding TPV deployment in image-derived, patient-specific RVOT geometries, with the long-term goal of informing patient candidacy and selection of the optimal device for an individual patient. We implemented this open-source capability in the SlicerHeart extension for 3D Slicer and FEBio [23–25]. Specific contributions include the demonstration of rapid machine learning-based segmentation of the RVOT and coronary arteries, a novel custom interface for TPV selection and positioning within the RVOT, and direct export from SlicerHeart into FEBio for simulation. We then demonstrate virtual TPV implantation of multiple devices in a range of RVOT morphologies and demonstrate visualization and quantification of device shape, compression, and vessel contact to inform optimal device placement in a given patient. Further development of this workflow could inform selection of the optimal TPVR in an individual patient and can be generalizable to any self-expanding medical device.

### 3 Methods

The modules and other code used for image segmentation are included in the SlicerHeart extension for 3D Slicer and are also available at [www.github.com/SlicerHeart](http://www.github.com/SlicerHeart) [23, 24]. The open-source finite element solver, FEBio version 4.7.0, was used for all FE simulations of TPV deployment [25]. The modeling workflow utilized is displayed in Figure 1.

#### 3.1 Subjects

An existing institutional database was used to retrospectively identify patients with a diagnosis of ToF who underwent TPVR and in whom computed tomography angiography (CTA) of the RVOT prior to TPVR had been previously acquired. Three patients with ToF (21.19, 16.40, and 13.72 years old) were chosen to demonstrate device deployment in RVOT of varying sizes and shapes. The Institutional Review Board at the Children’s Hospital of Philadelphia approved this study.

#### 3.2 Image Acquisition

A retrospective ECG-gated dual-source scanner (Siemens Healthineers, Forchheim, Germany) was used for image acquisition, with 2 x 128 x 0.6 mm slice collimation. 350 mg/mL Omnipaque (iohexol, GE Healthcare, Chicago, IL), a low-osmolar iodinated contrast, was injected via peripheral intravenous access at a dose of 2 mL/kg, up to 100 mL. The contrast was followed by an injection of normal saline using a dual-head power injector (Medrad Inc, Warrendale, PA). CTA images were available only for the diastolic phase for all three patients explored in this study. CTA images were imported into 3D Slicer ([www.slicer.org](http://www.slicer.org)) in Digital Imaging and Communications in Medicine (DICOM) format. CT images of three unconstrained TPV devices were acquired on the CT scanner to assist in the creation of realistic device models. In addition, measurements and dimensions were confirmed with Neiko 01407A digital calipers sensitive to 0.01 mm (Zhejiang Kangle Group, Wenzhou, China).

### 3.3 RVOT Segmentation

Initial segmentations were generated using threshold paint with 3D sphere brushes and manual revision using the Segment Editor module in 3D Slicer as previously described [10]. The sphere brushes were given a diameter of 2% of the screen size for changes that span multiple slices and 1% for finer edits on a single slice view. A deep learning-based model was trained to automatically segment the RVOT and coronary arteries, as previously described. MONAI’s DeepEdit was modified for this population [26] as we recently described [27]. During model training, the CT images went through a number of transforms for normalization and data augmentation to introduce more variation. All images were resampled to a resolution of 1mm x 1mm x 1mm. During preliminary observations, the intensity values of RVOT and coronary arteries were located in range 125-550 HU. The image intensities were thresholded to  $125 \leq I \leq 550$  HU and scaled to  $0.0 \leq I \leq 1.0$ , with  $I$  representing the image intensity. Data augmentation included random flips, intensity shifts, and 90-degree rotations. Finally, datasets were centrally cropped/padded to have a spatial size of 192 x 192 x 192.

Training was performed on 80 datasets for 50 epochs. As training advanced, the deep-learning model was utilized for the creation of further training samples with manual inspection and, if necessary, modification by a physician with prior segmentation experience (YBC). 100 models were created in total. Segmentations of the RVOT examples herein were made with deep learning and the MONAILabel module in 3D Slicer [28]. The segmentations were subsequently cleaned and smoothed in the Segment Editor module. RVOT segmentations were converted to models and the ends were uncapped using the Dynamic Modeler tool to form hollow models. The automatic segmentation process is shown in Video-1. Figure 2 shows the segmented RVOTs used for this study. The respective RVOT morphology types based on perimeter-derived diameters at different lengths along the RVOT [13] are also highlighted in 2.

### 3.4 TPVR Simulation Module Features

#### 3.4.1 Device Design

A custom TPVR Simulation module was developed in SlicerHeart to allow placement of a few widely available, commercial TPV devices into the RVOT [24]. The module currently supports positioning of the Harmony TPV-22 (Medtronic, Minneapolis, MN), Harmony TPV-25 (Medtronic, Minneapolis, MN), and the Alterra adaptive prestant (Edwards Lifesciences, Irvine, CA). Models of these devices were created in the Computer Aided Design software, Fusion 360 (Autodesk, San Francisco, CA), from CT imaging and measurements specified in the device documentation [29, 30]. All three TPV devices are made of Nitinol with shape-memory capabilities. The TPV-22 and TPV-25 wireframe devices were modeled with a wire diameter of 0.375 mm. The true Alterra device consists of a laser-cut frame; each wire-like piece has a rectangular cross-section with rounded edges and approximate dimensions of 0.25 mm by 0.32 mm. We modeled the Alterra with a round wire of diameter 0.32 mm for simplicity. We based this value on the diameter of a circle that yields the same cross-sectional area as the actual rectangular cross-section of the Alterra. The TPVs were remeshed as tetrahedral elements using TetWild [31] and GMSH [32], then integrated directly

into the TPVR Simulation module as .vtk files for easy user selection. Figure 2 also shows the TPV devices used in this study.

### 3.4.2 Device Positioning in Right Ventricular Outflow Tract

Figure 3 shows the procedure for device placement and the TPVR Simulation Module functionality. The TPVR Simulation module uses the vessel centerline and the central axis of the device to position the TPV in the RVOT. The vessel centerline was defined automatically using the Vascular Modeling Toolkit extension centerline extraction functionality or placed manually using an open curve in the Markups module [33] in 3D Slicer. Once a device has been selected, the device is snapped to the centerline for precise placement. If the device imports upside-down with respect to the RVOT model and associated CT image, there is a button to flip the device into the correct orientation while keeping it aligned with the centerline. The user can slide the TPV along the centerline using a slider control or by inputting a value representing the desired location along the centerline. The centerline has been discretized into sections with values from 0 to 100, with 0 corresponding to the most distal point and 100 representing the proximal endpoint. As the device is slid along the vessel centerline, the angle of the device automatically adjusts so that its vertical axis is tangent to the vessel centerline at the center of mass of the TPV. In addition, the TPV can be rotated or translated freely to refine pre-simulation placement. This can be done via menu sliders controlling orientation and spatial position or by using the 3D interactive handler and dragging the device. Should the user wish to change their device type or centerline at any point in the process, they can do so by returning to the Device Selection or Device Positioning subsection, respectively, and selecting a different one. Doing so will not alter the location of the TPV unless they then choose to move it. The device positioning and selection process is highlighted in Video-1.

### 3.4.3 Tube Creation for Simulation

To simulate uniform compression of the device prior to TPV expansion, we created a curved tube surface that surrounds the device using the vessel centerline and the MarkupsToModel extension, leveraging vtkTubeFilter [34]. The centerline curve points for the tube are interpolated using global least squares polynomial interpolation. The Centerline Parameters section of the module enables the user to toggle the visibility of the tube and set the radius and number of sides of the tube. The module accommodates radii values of 0 to 50 mm. We chose a radius for the tube that was sufficient to contain the device at the desired position and angle without penetrating the tube, usually 28 mm. The tube's mesh density depends on the number of points used to form the centerline and the number of sides. Increasing the number of sides adds more elements circumferentially. The number of elements spanning the tube vertically can be increased by resampling the centerline to have more points under Markups. Tube mesh density can be altered to prevent penetration of the device during simulations. Video-1 also highlights the tube creation process.

### 3.4.4 Export

After the TPV was positioned and the tube given an appropriate radius and mesh density, we exported the tube, TPV, and RVOT shell from the Import / Export subsection of the TPVR Simulation module. The module applies a transform to all selected components upon export so that the saved files are aligned along Z in global Cartesian coordinates. The Z axis corresponds to the vertical axis through the TPV. This facilitates the definition of local material axes and imposes constraints during simulation. The transformation can be undone by using the import feature when bringing the geometries back into 3D Slicer. The 3D Slicer scene was saved as a .mrb (medical reality bundle) file so it could be accessed later for visualization.

### 3.4.5 FEM Mesh Creation

For each patient case, the shell mesh representing the inner surface of the RVOT was exported from 3D Slicer as a stereolithography (.STL) file to be remeshed as quad elements in Blender (V4.4). These surfaces were reduced in density and meshed as quads with an average element size of 1.5 mm. This quad meshed RVOT surface was saved as a .ply format from Blender and subsequently imported into FEBio. The quad mesh was then extruded normally outward to have a thickness of 1.5 mm [35, 36]. The RVOT mesh was divided into four layers to replicate the orthotropic nature of the artery based on the results of a mesh convergence study observing strain in increasing numbers of layers. The final solid vessel geometries had between 24,000 and 32,000 elements, depending on the size of the vessel. The previously meshed TPV device .vtk and the tube .STL were brought into FEBio as well. The tube was converted to an editable mesh and assigned a shell thickness of 2.0 mm.

### 3.4.6 Simulation of Device Expansion

The simulation was divided into two analysis steps to capture the curved compression of the device, as though fitting it into the catheter delivery system, followed by the staged deployment in the vessel, as also shown in Figure 4. The distal half of the TPV device expands before the proximal half to mimic the delivery system sheath being pulled back and the device released. The tube was compressed over one second at a rate such that the enclosed device was well contained within the vessel. To achieve this, a displacement normal to the surface of the curved tube was applied to compress the device uniformly. Although the devices should fit within a delivery catheter system with a diameter of 8.33 mm (25 Fr) [29], we experienced instability in the models at very high compression due to complexities in the contact problem, so we used a larger target diameter of 16 mm after compression for this study. In most of our example cases, the compression rate was 20 mm/s, for the tube had an initial radius of 28 mm. When a greater initial radius was required for the tube to fully surround the device without penetration, the rate was adjusted accordingly to meet the same target radius. During TPV deployment, each half of the device was allowed to expand at the same rate at which it was compressed. The device compression and expansion simulation in FEBio is shown in Video-1.

The RVOT is incompressible and exhibits orthotropic material behavior at large deformations. We instituted an uncoupled Holzapfel-Gasser-Ogden (HGO) constitutive model for the RVOT to account for the fiber orientation and orthotropic nature of the RVOT vessels. The model uncouples the deviatoric and volumetric contributions in the strain-energy function:

$$\Psi_r = \tilde{\Psi}_r(\tilde{C}) + U(J) \quad (1)$$

with

$$\tilde{\Psi}_r = \frac{c}{2}(\tilde{I}_1 - 3) + \frac{k_1}{2k_2} \sum_{\alpha=1}^2 \left( \exp(k_2 \langle \tilde{E}_\alpha \rangle^2) - 1 \right) \quad (2)$$

and the volumetric portion

$$U(J) = \frac{k}{2} \left( \frac{J^2 - 1}{2} - \ln J \right) \quad (3)$$

$\tilde{I}_1 = \text{tr} \tilde{C}$ ,  $\tilde{I}_{4\alpha} = a_{\alpha r} \cdot \tilde{C} \cdot a_{\alpha r}$ , and  $\alpha = 1, 2$ .  $\tilde{C}$  is the right Cauchy-Green deformation tensor.

$E_\alpha = \kappa(\tilde{I}_1 - 3) + (1 - 3\kappa)(\tilde{I}_{4\alpha} - 1)$  represents the fiber strain [37, 38]. For parameters,  $k_1$  is the fiber modulus,  $k_2$  is the fiber exponential coefficient,  $k$  is the bulk modulus,  $\kappa$  is the fiber dispersion, and  $c$  is the shear modulus of the ground matrix. We used HGO material properties as defined in Donahue et al. [39].

We adopted the isotropic elastic material model [40] present in FEBio for the Nitinol TPV. The density, Young's modulus  $E$ , and Poisson's ratio  $\nu$  must be defined. We chose known material properties for Nitinol [41]. The Nitinol device had a density of 6.45e-06 kg/mm<sup>3</sup> and a Poisson's ratio of 0.33. Nitinol exhibits superelasticity, which means that its stiffness transitions from a stiff austenite phase to a softer martensite phase to accommodate the large strains experienced during compression. When a stent expands after being unloaded, the material undergoes a reverse transformation from martensite back to austenite, resulting in an increase in stiffness as it returns to its original shape. As such, a step function load curve was applied to the Young's modulus to simulate the transition of the effective stiffness in the device between the compression and release phases. The hyperelastic strain-energy function for the isotropic elastic material is given as:

$$W = \frac{1}{2} \lambda (\text{tr} E)^2 + \mu E : E \quad (4)$$

where  $E$  is the Euler-Lagrange strain tensor.  $\lambda$  and  $\mu$  are the Lamé parameters. The material parameters and those in the strain-energy function share the following relationship:

$$\mu = \frac{E}{2(1 + \nu)} \quad (5)$$

$$\lambda = \frac{\nu E}{(1 + \nu)(1 - 2\nu)} \quad (6)$$

While objective at large deformations, the model reduces to a linear elastic material for small strains.

We used an unconstrained Neo-Hookean material [42] for the tube that compresses the device. For simplicity, the tube was assigned parameter values identical to the TPV, but the Young’s modulus was kept constant at 40 GPa. The strain-energy function is

$$W = \frac{\mu}{2}(I_1 - 3) - \mu \ln(J) + \frac{\lambda}{2}(\ln J)^2 \quad (7)$$

where  $C$  is the right Cauchy-Green deformation tensor,  $I_1$  and  $I_2$  are the first and second invariants of  $C$ , and  $J$  is the determinant of the deformation gradient tensor. The model captures the non-linear stress-strain response but reduces to classical linear elasticity under small strains and small rotations [43].

Boundary conditions and contacts were imposed on all geometries but varied by step. A potential-based contact formulation was used to constrain the TPV to stay within the tube during compression and staged expansion [44, 45]. The same contact formulation was used between the TPV and the vessel during deployment of the device within the RVOT. A zero displacement boundary condition was imposed on the central nodes of the TPV to prevent sliding along the vertical Z axis. The ends of the vessel were fixed. Expansion of the TPV was controlled by a normal displacement boundary condition applied to the surrounding tube and by the enforced contact potential, mimicking the self-expanding behavior of the Nitinol devices. To improve the stability of the simulation, mass damping was assigned to the device as part of a false transient approach.

### 3.4.7 Visualization of Results

Device and RVOT metrics were visualized by exporting the expanded device and vessel from FEBio and importing them in 3D Slicer using the import section of the TPVR simulation module. After importing the mesh into Slicer, metrics calculated by FEBio were pre-processed so that they could be visualized on the vessel and model surface mesh. For vector metrics such as displacement, we computed the length of the displacement vector and visualized the magnitude of the vector on each point in the mesh. In metrics such as stress, we computed and visualized the absolute magnitude of the eigenvalues for each polygon in the mesh. The metric pre-processing generated single-component values for the metrics that were visualized by applying a scalar overlay on the mesh, coloring the surface based on the metric value.

To visualize the contact between the device and vessel, we calculated a B-spline transformation using the ScatteredTransform extension in 3D Slicer. The B-spline transformation reflects the deformation of the device mesh from its original location to its final position at the end of the FEBio simulation. We then applied the same deformation to a mesh of the fabric for the corresponding device. The distance between this deformed fabric mesh and the vessel wall was calculated using the ModelToModel distance extension in 3D Slicer. The absolute distance from the points in the device fabric mesh to the closest point on the vessel wall was calculated for each point in the fabric mesh, and vice versa. To visualize regions of contact, we applied a color gradient to the model representing the distance between the fabric and vessel mesh. We also hid

or reduced the opacity of regions that were not within a specified distance threshold to highlight the regions of contact between the device fabric and the vessel wall.

### 3.4.8 Quantitative Metrics of Compression

Quantitative compression metrics included the 1st principal Lagrangian strain, 1st principal stress, and percentage contact area of the valve frame in the proximal and distal halves of the vessel at complete device expansion. The 99th percentile, 75th percentile, and maximum 1st principal Lagrangian strain and stress were plotted for each device and patient. The percentage of the total device area in contact with the vessel wall was calculated for the proximal and distal halves to determine the proximal and distal seal for each device.

## 4 Results

Time taken for automatic segmentation of the RVOT models was 5 seconds. Time taken for device placement was 45 seconds. The average computational time was 2 hr 17 min for simulations with the TPV-25 and 5 hr 34 min for the Alterra on an Intel Core i9 10980 XE CPU @ 3.00GHz processor with 64.0 GB RAM system. The Alterra model required more elements than the TPV-25 due to a more complex shape, which contributed to an elevated runtime.

The distribution of stress, strain, and stent-vessel contact is critical for evaluating device fit, mechanical stability, and potential risk of complications. High local stresses and strains in the vessel wall can indicate areas at risk for tissue injury, vessel remodeling, or even rupture, particularly important in fragile or surgically repaired RVOTs. Conversely, insufficient mechanical interaction (i.e., low strain or minimal contact) may suggest suboptimal anchoring of the device, increasing the risk of stent migration or paravalvular leak. To evaluate device fit, we examined the 1st principal strain and stress, as well as areas of contact between each stent and vessel. All quantitative metrics of compression have been depicted in Video-2. We divided the stent centrally about its vertical axis into proximal and distal halves in order to assess proximal and distal device compression separately.

Figures 5 and 6 highlight the 1st principal Lagrangian strain and 1st principal stress distribution across the three RVOT models when the TPV-25 and Alterra devices are fully expanded, as well as the 99th percentile, 75th percentile, and maximum values of those strains and stresses. Areas of high stress and strain were observed at the proximal and distal ends of the RVOTs, where the device wireframes contact the RVOT vessel wall and where the device geometries are the broadest.

Across these three RVOT models, the 75th percentile strain and stress values were fairly similar between the two stents. For RVOT4, the TPV-25 resulted in greater 99th percentile and maximum strain and stress than the Alterra. For both stents, strain and stress at the proximal and distal halves of the RVOT were similar. For RVOT12, like RVOT4, the TPV-25 produced a greater 99th percentile and maximum strain and stress than the Alterra. Proximal and distal strains and stresses were similar. In RVOT28, trends varied from RVOTs 4 and 12. At the proximal half, TPV-25 resulted in greater 99th percentile strain and stress, but lesser maximum strain and stress than

the Alterra. At the distal half of the RVOT, TPV-25 produced a lower 99th percentile and maximum strain and stress than the Alterra. On comparing the two halves, the distal half of RVOT28 showed greater strain and stress values than the proximal half across both stents, except for the maximum stress when the TPV-25 was used.

Contact maps generated for each RVOT and stent condition are shown in figure 7. Greater contact was observed at the proximal and distal ends of the RVOT where the stent geometries are the broadest. Overall, the TPV-25 had a greater percentage of the total stent area in contact with the vessel walls than the Alterra. On analyzing by location, the TPV-25 had fairly similar contact percentages in the proximal and distal halves. However, for RVOTs 4 and 12, the Alterra device contacted only 1% and 6% of its proximal area of the stent in the proximal half. For the Alterra stent, contact percentages in the distal half were much greater than those in the proximal half, unlike the TPV-25 stent.

By quantifying and comparing stress, strain, and contact patterns across multiple patient-specific anatomies and devices, this study underscores the importance of personalized anatomical reconstruction in TPVR. The observed variability in these metrics across different RVOTs, between stents (TPV-25 vs. Alterra), and locations in the RVOT (proximal vs. distal) highlights that no single device performs optimally in all anatomies, reinforcing the need for simulation-driven preprocedural assessment.

## 5 Discussion

In this study, we developed an integrated workflow to model TPV deployment in patient-specific, image-derived RVOT anatomies, with the long-term goal of improving patient selection and device fit for TPVR. The workflow incorporates automated RVOT segmentation, interactive TPV selection and placement through a dedicated SlicerHeart module, followed by simulation of device–tissue interaction using FEBio. We evaluated two commonly used TPVs across three distinct patient anatomies, assessing first principal stress, strain distributions, and regions of contact to determine device fit.

While image-based simulations are increasingly used to support adult structural interventions, similar workflows have yet to be routinely adopted in congenital heart disease. [46–48] However, patient-specific modeling may be especially valuable in this setting due to the high anatomical variability and small patient cohorts, which limit the feasibility of large clinical trials and empirical design validation.

Several groups have explored the modeling of TPVR over the last two decades, which laid the groundwork for the current generation of patient-specific simulations. Capelli et al. [15, 49] pioneered early simulations of self-expanding devices in image-derived RVOT models, laying the foundation for later studies. Their early implementations assumed a rigid, non-deformable RVOT, now recognized as a significant simplification [10]. Bosi et al. [50] advanced the field by introducing deformable vessel behavior and simulating both balloon-expandable and self-expanding valves using Abaqus, though with simplified isotropic linear elastic models for the vessel wall. Further advancements have aimed to improve the physiological accuracy of vessel mechanics. Donahue et al. [39], for example, applied the Holzapfel-Gasser-Ogden

(HGO) constitutive model to account for anisotropy and fiber orientation in RVOT tissue. However, their work focused on simulating balloon expansion through wall pressurization to assess coronary compression risk, rather than modeling the deployment of a self-expanding TPV device.

Notably, these foundational simulations predated the commercial availability of dedicated self-expanding TPV devices for pediatric patients. In this study, we address that gap by simulating the deployment of commercially available self-expanding TPVs in a range of pediatric RVOT anatomies. Using the HGO model to represent the RVOT wall, we demonstrate the feasibility of preprocedural prediction of device expansion, positioning, and vessel interaction in patient-specific cases. To further enhance the practicality of our workflow, we incorporated machine-learning-based segmentation for automated RVOT extraction. While now increasingly routine, this capability greatly improves efficiency and supports the clinical applicability of patient-specific modeling, particularly in complex congenital anatomies [27].

Comparing the stress, strain, and contact patterns across the three RVOTs and two stents explored in this study highlights that no single device performs optimally in all anatomies. Although the Alterra device results in a smaller percentage contact area of the stent compared to the TPV-25, this can be attributed to the design of the device. The Alterra device has tines at its proximal and distal ends, which embed into the RVOT wall on installation. Scar tissue developing around the area where the stent's tines impinge the RVOT wall seemingly results in strong placement of the device. However, this behavior is not captured in our simulations. Associating the stress, strain, and contact patterns for a cohort of patients for whom this procedure was successful or unsuccessful would provide data to link these mechanical measures to actual clinical outcomes.

Despite the strengths of our integrated approach, including automatic segmentation, TPV selection, and direct export to FEBio for soft tissue interaction modeling, several limitations remain. First, the simulations focus solely on biomechanical outcomes and do not incorporate blood flow or hemodynamic forces. Future work will incorporate fluid–structure interaction (FSI) modeling to enable more comprehensive predictions. That said, our current models do simulate vascular pressurization, allowing us to capture the combined effects of TPV insertion and vessel deformation, and approximate physiologic conditions reasonably well.

Device–tissue interaction was modeled using a contact potential method, based on the formulation by Kamensky et al. [44], which applies a repulsive force when surfaces come within a specified distance. Although this approach maintains an artificial small gap between the stent and vessel wall, it prevents penetration and offers a more stable solution compared to the sliding-elastic formulation in FEBio, especially for soft tissue interactions [25].

Notably, the material phase transformation in the Nitinol stent is influenced by the progression of the martensitic volume fraction, which changes in response to internal stress during deformation. Although our step-function approach provides a reasonable approximation of the overall characteristics of the stent, it does not fully capture the mechanical hysteresis behavior associated with the transformation. Subsequent work will aim to implement a more physically representative superelasticity model [51] based

on the martensite fraction, similar to those presented in previous literature [52–54]. A more representative material model for the stent may result in different softening and stiffening mechanisms that could influence the final expansion of the stent, and the strain and stress values and distribution in the RVOT. However, this needs to be explored further.

Simulation run times were relatively long due to the use of solid elements in modeling the TPV device. As a next step, we plan to integrate 1-dimensional beam elements, which are expected to reduce computational cost while more effectively capturing the bending behavior of the stent.

In our simulations, the RVOT wall was modeled using HGO parameters from existing literature [39], without accounting for layer-specific material properties due to the lack of experimental data in pediatric tissues. Currently, tissue-derived material data for the pulmonary artery are limited to a small number of patients, ranging in age from infancy [55] to older adults [56]. Non-conduit RVOTs, which include both native (non-patched) and surgically patched RVOTs, have anatomies that are categorized by substantial heterogeneity in geometry and biomechanical properties. These include unpredictable tissue compliance and distensibility. A comprehensive sensitivity analysis of RVOT material parameters may help understand the variation observed in RVOT behavior due to device expansion. Given the difficulty of in vivo mechanical characterization and expected interpatient variability of vessel wall parameters, simulation accuracy will continue to improve as new tissue mechanical testing data and novel measurement techniques become available [57].

CTA images, and hence, the RVOT geometries of all three patients, corresponded to the diastolic phase. Prior literature has reported that the phase of the CT dataset is crucial for assessing device stability [58]. While the use of the diastolic phase for analysis may have a negligible impact in the context of conduit RVOTs, its influence in non-conduit RVOTs, where compliance and dynamic dimensional changes are more pronounced, could be more substantial and needs to be explored further. Since the RVOT and pulmonary artery are dynamic, future simulations will include both diastolic and systolic models to allow comparison over the cardiac cycle.

Finally, another limitation of this study is the small sample size and lack of validation against clinical post-implantation geometries. Typically, post-implantation CTA scans in patients undergoing these procedures are performed only if there is a device functionality failure. Although the goal of this study was to present an end-to-end device compatibility workflow, future work will include a larger cohort and comparisons with post-procedural imaging to evaluate predictive accuracy.

## 6 Conclusion

The open-source and adaptable nature of our platform makes it well-suited for continued advancement and broader application. By enabling the development and testing of patient-specific workflows, it provides a foundation for evaluating both novel devices and new uses of existing technologies [59]. With ongoing refinement and validation, this framework has the potential to become a valuable clinical tool for optimizing device selection and guiding procedural planning in TPVR.

**Acknowledgements.** This work was supported by NIH R01HL153166, K25HL168235, 2R01GM083925, a CHOP Cardiac Center Innovation Award, the Topolewski Pediatric Valve Center at CHOP, and a CHOP Research Institute Post-Frontier Award.

## Declarations

Matthew J. Gillespie is a consultant for Medtronic. The other authors have no disclosures.

## References

- [1] Stallings, E.B., Isenburg, J.L., Rutkowski, R.E., Kirby, R.S., Nembhard, W.N., Sandidge, T., Villavicencio, S., Nguyen, H.H., McMahon, D.M., Nestoridi, E., Pabst, L.J., for the National Birth Defects Prevention Network: National population-based estimates for major birth defects, 2016–2020 **116**(1), 2301 <https://doi.org/10.1002/bdr2.2301> . Accessed 2025-06-06
- [2] Geva, T., Mulder, B., Gauvreau, K., Babu-Narayan, S.V., Wald, R.M., Hickey, K., Powell, A.J., Gatzoulis, M.A., Valente, A.M.: Preoperative predictors of death and sustained ventricular tachycardia after pulmonary valve replacement in patients with repaired tetralogy of fallot enrolled in the INDICATOR cohort **138**(19), 2106–2115 <https://doi.org/10.1161/CIRCULATIONAHA.118.034740>
- [3] Bokma, J.P., Geva, T., Sleeper, L.A., Lee, J.H., Lu, M., Sompolinsky, T., Babu-Narayan, S.V., Wald, R.M., Mulder, B.J.M., Valente, A.M.: Improved outcomes after pulmonary valve replacement in repaired tetralogy of fallot **81**(21), 2075–2085 <https://doi.org/10.1016/j.jacc.2023.02.052>
- [4] Bokma, J.P., Geva, T., Sleeper, L.A., Babu Narayan, S.V., Wald, R., Hickey, K., Jansen, K., Wassall, R., Lu, M., Gatzoulis, M.A., Mulder, B.J., Valente, A.M.: A propensity score-adjusted analysis of clinical outcomes after pulmonary valve replacement in tetralogy of fallot **104**(9), 738–744 <https://doi.org/10.1136/heartjnl-2017-312048>
- [5] Valente, A.M., Gauvreau, K., Assenza, G.E., Babu-Narayan, S.V., Schreier, J., Gatzoulis, M.A., Groenink, M., Inuzuka, R., Kilner, P.J., Koyak, Z., Landzberg, M.J., Mulder, B., Powell, A.J., Wald, R., Geva, T.: Contemporary predictors of death and sustained ventricular tachycardia in patients with repaired tetralogy of fallot enrolled in the INDICATOR cohort **100**(3), 247–253 <https://doi.org/10.1136/heartjnl-2013-304958>
- [6] Law, M.A., Chatterjee, A.: Transcatheter pulmonic valve implantation: Techniques, current roles, and future implications **13**(5), 117–129 <https://doi.org/10.4330/wjc.v13.i5.117> . Accessed 2025-06-06

- [7] Gillespie, M.J., McElhinney, D.B., Jones, T.K., Levi, D.S., Asnes, J., Gray, R.G., Cabalka, A.K., Fujimoto, K., Qureshi, A.M., Justino, H., Bergersen, L., Benson, L.N., Haugan, D., Boe, B.A., Cheatham, J.P.: 1-year outcomes in a pooled cohort of harmony transcatheter pulmonary valve clinical trial participants **16**(15), 1917–1928 <https://doi.org/10.1016/j.jcin.2023.03.002> . Accessed 2025-06-06
- [8] Crago, M., Winlaw, D.S., Farajikhah, S., Dehghani, F., Naficy, S.: Pediatric pulmonary valve replacements: Clinical challenges and emerging technologies **8**(4), 10501 <https://doi.org/10.1002/btm2.10501> . Accessed 2025-06-06
- [9] Gartenberg, A.J., Gillespie, M.J., Glatz, A.C.: Transcatheter approaches to pulmonary valve replacement in congenital heart disease: Revolutionizing the management of RVOT dysfunction? **35**(2), 333–338 <https://doi.org/10.1053/j.semtcvs.2022.02.009> . Accessed 2025-06-06
- [10] Jolley, M.A., Lasso, A., Nam, H.H., Dinh, P.V., Scanlan, A.B., Nguyen, A.V., Ilina, A., Morray, B., Glatz, A.C., McGowan, F.X., Whitehead, K., Dori, Y., Gorman, J.H., Gorman, R.C., Fichtinger, G., Gillespie, M.J.: Toward predictive modeling of catheter-based pulmonary valve replacement into native right ventricular outflow tracts **93**(3), 143–152 <https://doi.org/10.1002/ccd.27962>
- [11] Kenny, D.P., Hijazi, Z.M.: Current status and future potential of transcatheter interventions in congenital heart disease **120**(6), 1015–1026 <https://doi.org/10.1161/CIRCRESAHA.116.309185> . Accessed 2025-06-06
- [12] Patel, N.D., Levi, D.S., Cheatham, J.P., Qureshi, S.A., Shahanavaz, S., Zahn, E.M.: Transcatheter pulmonary valve replacement: A review of current valve technologies **1**(6), 100452 <https://doi.org/10.1016/j.jscai.2022.100452> . Accessed 2025-06-06
- [13] Schievano, S., Coats, L., Migliavacca, F., Norman, W., Frigiola, A., Deanfield, J., Bonhoeffer, P., Taylor, A.M.: Variations in right ventricular outflow tract morphology following repair of congenital heart disease: implications for percutaneous pulmonary valve implantation **9**(4), 687–695 <https://doi.org/10.1080/10976640601187596>
- [14] Odemis, E., Aka, .I.B., Kızılkaya, M.H.: 3d modeling of self-expandable valves for PPVI in distinct RVOT morphologies <https://doi.org/10.1007/s00246-025-03796-7>
- [15] Capelli, C., Taylor, A.M., Migliavacca, F., Bonhoeffer, P., Schievano, S.: Patient-specific reconstructed anatomies and computer simulations are fundamental for selecting medical device treatment: application to a new percutaneous pulmonary valve **368**(1921), 3027–3038 <https://doi.org/10.1098/rsta.2010.0088> . Accessed 2025-06-06

- [16] Benson, L.N., Gillespie, M.J., Bergersen, L., Cheatham, S.L., Hor, K.N., Horlick, E.M., Weng, S., McHenry, B.T., Osten, M.D., Powell, A.J., Cheatham, J.P.: Three-year outcomes from the harmony native outflow tract early feasibility study **13**(1), 008320 <https://doi.org/10.1161/CIRCINTERVENTIONS.119.008320>
- [17] Zahn, E.M., Chang, J.C., Armer, D., Garg, R.: First human implant of the alterra adaptive PreStent™ : A new self-expanding device designed to remodel the right ventricular outflow tract **91**(6), 1125–1129 <https://doi.org/10.1002/ccd.27581>
- [18] Jin, Q., Long, Y., Zhang, G., Pan, X., Chen, M., Feng, Y., Liu, J., Yu, S., Pan, W., Zhou, D., Ge, J.: Five-year follow-up after percutaneous pulmonary valve implantation using the venus p-valve system for patients with pulmonary regurgitation and an enlarged native right ventricular outflow tract **103**(2), 359–366 <https://doi.org/10.1002/ccd.30916>
- [19] Schoonbeek, R.C., Takebayashi, S., Aoki, C., Shimaoka, T., Harris, M.A., Fu, G.L., Kim, T.S., Dori, Y., McGarvey, J., Litt, H., Bouma, W., Zsido, G., Glatz, A.C., Rome, J.J., Gorman, R.C., Gorman, J.H., Gillespie, M.J.: Implantation of the medtronic harmony transcatheter pulmonary valve improves right ventricular size and function in an ovine model of postoperative chronic pulmonary insufficiency **9**(10), 003920 <https://doi.org/10.1161/CIRCINTERVENTIONS.116.003920>
- [20] Gillespie, M.J., Benson, L.N., Bergersen, L., Bacha, E.A., Cheatham, S.L., Crean, A.M., Eicken, A., Ewert, P., Geva, T., Hellenbrand, W.E., Hor, K.N., Horlick, E.M., Jones, T.K., Mayer, J., McHenry, B.T., Osten, M.D., Powell, A.J., Zahn, E.M., Cheatham, J.P.: Patient selection process for the harmony transcatheter pulmonary valve early feasibility study **120**(8), 1387–1392 <https://doi.org/10.1016/j.amjcard.2017.07.034>
- [21] McElhinney, D.B., Gillespie, M.J., Aboulhosn, J.A., Cabalka, A.K., Morray, B.H., Balzer, D.T., Qureshi, A.M., Hoskoppal, A.K., Goldstein, B.H.: Transcatheter pulmonary valve replacement with the harmony valve in patients who do not meet recommended oversizing criteria on the screening perimeter plot **17**(5), 013889 <https://doi.org/10.1161/CIRCINTERVENTIONS.123.013889>
- [22] Bergersen, L., Benson, L.N., Gillespie, M.J., Cheatham, S.L., Crean, A.M., Hor, K.N., Horlick, E.M., Lung, T.-H., McHenry, B.T., Osten, M.D., Powell, A.J., Cheatham, J.P.: Harmony feasibility trial: Acute and short-term outcomes with a self-expanding transcatheter pulmonary valve **10**(17), 1763–1773 <https://doi.org/10.1016/j.jcin.2017.05.034>
- [23] Fedorov, A., Beichel, R., Kalpathy-Cramer, J., Finet, J., Fillion-Robin, J.-C., Pujol, S., Bauer, C., Jennings, D., Fennessy, F., Sonka, M., Buatti, J., Aylward, S., Miller, J.V., Pieper, S., Kikinis, R.: 3d slicer as an image computing platform for the quantitative imaging network **30**(9), 1323–1341 <https://doi.org/10.1016/j.mri.2012.05.001>

- [24] Lasso, A., Herz, C., Nam, H., Cianciulli, A., Pieper, S., Drouin, S., Pinter, C., St-Onge, S., Vigil, C., Ching, S., Sunderland, K., Fichtinger, G., Kikinis, R., Jolley, M.A.: SlicerHeart: An open-source computing platform for cardiac image analysis and modeling **9**, 886549 <https://doi.org/10.3389/fcvm.2022.886549> . Accessed 2025-06-06
- [25] Maas, S.A., Ellis, B.J., Ateshian, G.A., Weiss, J.A.: FEBio: Finite elements for biomechanics **134**(1), 011005 <https://doi.org/10.1115/1.4005694> . Accessed 2025-06-06
- [26] Diaz-Pinto, A., Mehta, P., Alle, S., Asad, M., Brown, R., Nath, V., Ihsani, A., Antonelli, M., Palkovics, D., Pinter, C., Alkalay, R., Pieper, S., Roth, H.R., Xu, D., Dogra, P., Vercauteren, T., Feng, A., Quraini, A., Ourselin, S., Cardoso, M.J.: DeepEdit: Deep editable learning for interactive segmentation of 3d medical images. In: Nguyen, H.V., Huang, S.X., Xue, Y. (eds.) Data Augmentation, Labelling, and Imperfections vol. 13567, pp. 11–21. Springer. [https://doi.org/10.1007/978-3-031-17027-0\\_2](https://doi.org/10.1007/978-3-031-17027-0_2) . Series Title: Lecture Notes in Computer Science. [https://link.springer.com/10.1007/978-3-031-17027-0\\_2](https://link.springer.com/10.1007/978-3-031-17027-0_2) Accessed 2025-06-07
- [27] Barak-Corren, Y., Obsekov, V., Gupta, M., Herz, C., Amin, S., Lasso, A., O’Byrne, M.L., Gillespie, M.J., Jolley, M.A.: Image-derived modeling to assess coronary proximity in patients undergoing transcatheter pulmonary valve replacement with self-expanding valves **105**(6), 1479–1485 <https://doi.org/10.1002/ccd.31469>
- [28] Diaz-Pinto, A., Alle, S., Nath, V., Tang, Y., Ihsani, A., Asad, M., Pérez-García, F., Mehta, P., Li, W., Flores, M., Roth, H.R., Vercauteren, T., Xu, D., Dogra, P., Ourselin, S., Feng, A., Cardoso, M.J.: MONAI label: A framework for AI-assisted interactive labeling of 3d medical images **95**, 103207 <https://doi.org/10.1016/j.media.2024.103207> . Accessed 2025-06-07
- [29] Medtronic: TPV 22 and TPV 25 Transcatheter Pulmonary Valves and Delivery Catheter System. [https://www.accessdata.fda.gov/cdrh\\_docs/pdf20/P200046D.pdf](https://www.accessdata.fda.gov/cdrh_docs/pdf20/P200046D.pdf)
- [30] Lifesciences, E.: Edwards SAPIEN 3 Transcatheter Pulmonary Valve System with Alterra Adaptive Presept. [https://www.accessdata.fda.gov/cdrh\\_docs/pdf20/P200015S011D.pdf](https://www.accessdata.fda.gov/cdrh_docs/pdf20/P200015S011D.pdf)
- [31] Hu, Y., Zhou, Q., Gao, X., Jacobson, A., Zorin, D., Panozzo, D.: Tetrahedral meshing in the wild **37**(4), 1–14 <https://doi.org/10.1145/3197517.3201353> . Accessed 2025-06-06
- [32] Geuzaine, C., Remacle, J.: Gmsh: A 3-d finite element mesh generator with built-in pre- and post-processing facilities **79**(11), 1309–1331 <https://doi.org/10.1002/nme.2579> . Accessed 2025-06-06

- [33] Piccinelli, M., Veneziani, A., Steinman, D.A., Remuzzi, A., Antiga, L.: A framework for geometric analysis of vascular structures: application to cerebral aneurysms **28**(8), 1141–1155 <https://doi.org/10.1109/TMI.2009.2021652>
- [34] Schroeder, W., Martin, K., Lorensen, B.: The Visualization Toolkit: An Object-Oriented Approach to 3D Graphics, 4th Edition. Kitware. <https://vtk.org/vtk-textbook/>
- [35] Donahue, C.L., Westman, C.L., Faanes, B.L., Qureshi, A.M., Barocas, V.H., Aggarwal, V.: Finite element modeling with patient-specific geometry to assess clinical risks of percutaneous pulmonary valve implantation **103**(6), 924–933 <https://doi.org/10.1002/ccd.31016> . Accessed 2025-06-06
- [36] Vanderveken, E., Vastmans, J., Claus, P., Verbeken, E., Fehervary, H., Van Hoof, L., Vandendriessche, K., Verbrugge, P., Famaey, N., Rega, F.: Mechano-biological adaptation of the pulmonary artery exposed to systemic conditions **10**(1), 2724 <https://doi.org/10.1038/s41598-020-59554-7> . Accessed 2025-06-06
- [37] Gasser, T.C., Ogden, R.W., Holzapfel, G.A.: Hyperelastic modelling of arterial layers with distributed collagen fibre orientations **3**(6), 15–35 <https://doi.org/10.1098/rsif.2005.0073> . Accessed 2025-06-06
- [38] Maas, S.A., Ateshian, G.A., Weiss, J.A., Herron, M.: Uncoupled Holzapfel-Gasser-Ogden. FEBio User’s Manual 4.9. <https://help.febio.org/docs/FEBioUser-4-9/UM49-4.1.2.8.html>
- [39] Donahue, C.L., Aggarwal, V., Barocas, V.H.: Finite element modeling using patient-specific geometry to predict aortic valve insufficiency during percutaneous pulmonary valve implantation. In: 2022 Design of Medical Devices Conference, pp. 001–02001. American Society of Mechanical Engineers. <https://doi.org/10.1115/DMD2022-1022> . <https://asmedigitalcollection.asme.org/BIOMED/proceedings/DMD2022/84815/V001T02A001/1140616> Accessed 2025-06-06
- [40] Maas, S.A., Ateshian, G.A., Weiss, J.A., Herron, M.: Isotropic Elastic. FEBio User’s Manual 4.9. <https://help.febio.org/docs/FEBioUser-4-9/UM49-4.1.4.14.html>
- [41] Vemury, C.M., Corradi, M., Abozaid, F., Charles, A., Hughes, D.: The behaviour of nitinol wire bundles for structural applications **03**(1), 1–1 <https://doi.org/10.21926/rpm.2101009> . Accessed 2025-06-06
- [42] Maas, S.A., Ateshian, G.A., Weiss, J.A., Herron, M.: Neo-Hookean. FEBio User’s Manual 4.9. <https://help.febio.org/docs/FEBioUser-4-9/UM49-4.1.4.19.html>
- [43] Bonet, J., Wood, R.D.: Nonlinear Continuum Mechanics for Finite Element Analysis, Second Edition. Cambridge University Press

- [44] Kamensky, D., Xu, F., Lee, C.-H., Yan, J., Bazilevs, Y., Hsu, M.-C.: A contact formulation based on a volumetric potential: Application to isogeometric simulations of atrioventricular valves **330**, 522–546 <https://doi.org/10.1016/j.cma.2017.11.007> . Accessed 2025-06-06
- [45] Maas, S.A., Ateshian, G.A., Weiss, J.A., Herron, M.: Contact Potential. FEBio User’s Manual 4.9. <https://help.febio.org/docs/FEBioUser-4-9/UM49-Subsection-3.14.10.html>
- [46] Xuan, Y., Krishnan, K., Ye, J., Dvir, D., Guccione, J.M., Ge, L., Tseng, E.E.: Stent and leaflet stresses in a 26-mm first-generation balloon-expandable transcatheter aortic valve **153**(5), 1065–1073 <https://doi.org/10.1016/j.jtcvs.2016.12.016>
- [47] Brown, J.A., Lee, J.H., Smith, M.A., Wells, D.R., Barrett, A., Puelz, C., Vavalle, J.P., Griffith, B.E.: Patient-specific immersed finite element-difference model of transcatheter aortic valve replacement **51**(1), 103–116 <https://doi.org/10.1007/s10439-022-03047-3>
- [48] Grossi, B., Barati, S., Ramella, A., Migliavacca, F., Rodriguez Matas, J.F., Dubini, G., Chakfé, N., Heim, F., Cozzi, O., Condorelli, G., Stefanini, G.G., Luraghi, G.: Validation evidence with experimental and clinical data to establish credibility of TAVI patient-specific simulations **182**, 109159 <https://doi.org/10.1016/j.combiomed.2024.109159> . Accessed 2025-06-17
- [49] Capelli, C., Bosi, G.M., Cerri, E., Nordmeyer, J., Odenwald, T., Bonhoeffer, P., Migliavacca, F., Taylor, A.M., Schievano, S.: Patient-specific simulations of transcatheter aortic valve stent implantation **50**(2), 183–192 <https://doi.org/10.1007/s11517-012-0864-1> . Accessed 2025-06-07
- [50] Bosi, G.M., Capelli, C., Khambadkone, S., Taylor, A.M., Schievano, S.: Patient-specific finite element models to support clinical decisions: A lesson learnt from a case study of percutaneous pulmonary valve implantation **86**(6), 1120–1130 <https://doi.org/10.1002/ccd.25944> . Accessed 2025-06-07
- [51] Auricchio, F., Taylor, R.L.: Shape-memory alloys: modelling and numerical simulations of the finite-strain superelastic behavior **143**(1), 175–194 [https://doi.org/10.1016/S0045-7825\(96\)01147-4](https://doi.org/10.1016/S0045-7825(96)01147-4) . Accessed 2025-06-11
- [52] Auricchio, F., Conti, M., De Beule, M., De Santis, G., Verheghe, B.: Carotid artery stenting simulation: From patient-specific images to finite element analysis **33**(3), 281–289 <https://doi.org/10.1016/j.medengphy.2010.10.011> . Accessed 2025-06-11
- [53] Tzamtzis, S., Viquerat, J., Yap, J., Mullen, M.J., Burriesci, G.: Numerical analysis of the radial force produced by the medtronic-CoreValve and edwards-SAPIEN after transcatheter aortic valve implantation (TAVI) **35**(1), 125–130 <https://doi.org/10.1016/j.jtcvs.2016.12.016>

[org/10.1016/j.medengphy.2012.04.009](https://doi.org/10.1016/j.medengphy.2012.04.009) . Accessed 2025-06-11

- [54] Maleckis, K., Anttila, E., Aylward, P., Poulson, W., Desyatova, A., MacTaggart, J., Kamenskiy, A.: Nitinol stents in the femoropopliteal artery: A mechanical perspective on material, design, and performance **46**(5), 684–704 <https://doi.org/10.1007/s10439-018-1990-1> . Accessed 2025-06-11
- [55] Cabrera, M.S., Oomens, C.W.J., Bouten, C.V.C., Bogers, A.J.J.C., Hoerstrup, S.P., Baaijens, F.P.T.: Mechanical analysis of ovine and pediatric pulmonary artery for heart valve stent design **46**(12), 2075–2081 <https://doi.org/10.1016/j.jbiomech.2013.04.020> . Accessed 2025-06-07
- [56] Holzapfel, G.A., Sommer, G., Gasser, C.T., Regitnig, P.: Determination of layer-specific mechanical properties of human coronary arteries with nonatherosclerotic intimal thickening and related constitutive modeling **289**(5), 2048–2058 <https://doi.org/10.1152/ajpheart.00934.2004>
- [57] Wu, W., Daneker, M., Herz, C., Dewey, H., Weiss, J.A., Pouch, A.M., Lu, L., Jolley, M.A.: A noninvasive method for determining elastic parameters of valve tissue using physics-informed neural networks, 1742706125003472 <https://doi.org/10.1016/j.actbio.2025.05.021> . Accessed 2025-06-10
- [58] Sturla, F., Caimi, A., Giugno, L., Pasqualin, G., Tissir, K., Secchi, F., Redaelli, A., Carminati, M., Votta, E.: Planning transcatheter pulmonary valve implantation in the dysfunctional native RVOT: A semi-automated pipeline for dynamic analysis based on 4d-CT imaging **260**, 108569 <https://doi.org/10.1016/j.cmpb.2024.108569> . Accessed 2025-11-06
- [59] Tsao, A.L., Colello, S., Gillespie, M.J.: Transcatheter repair of a sinus venosus defect with a modified harmony transcatheter pulmonary valve prosthesis **30**(9), 103294 <https://doi.org/10.1016/j.jaccas.2025.103294>

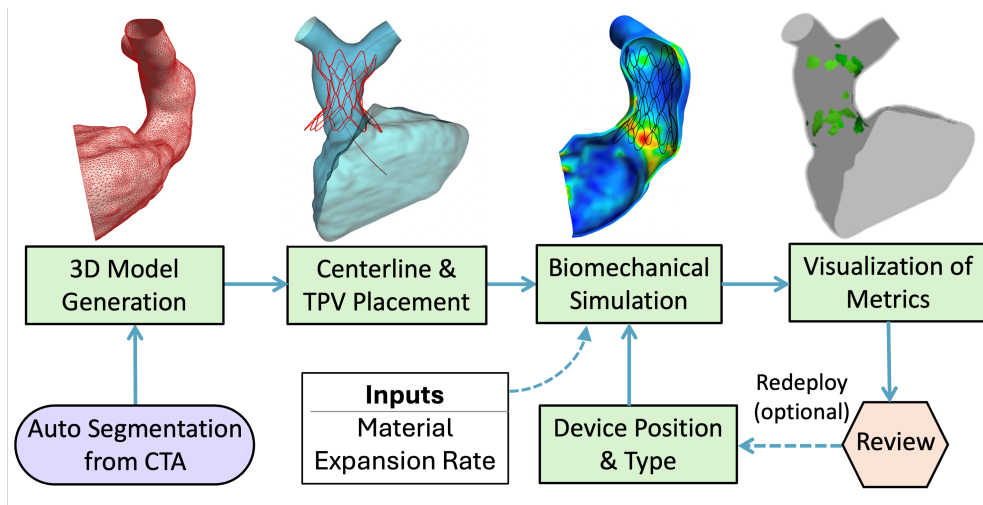
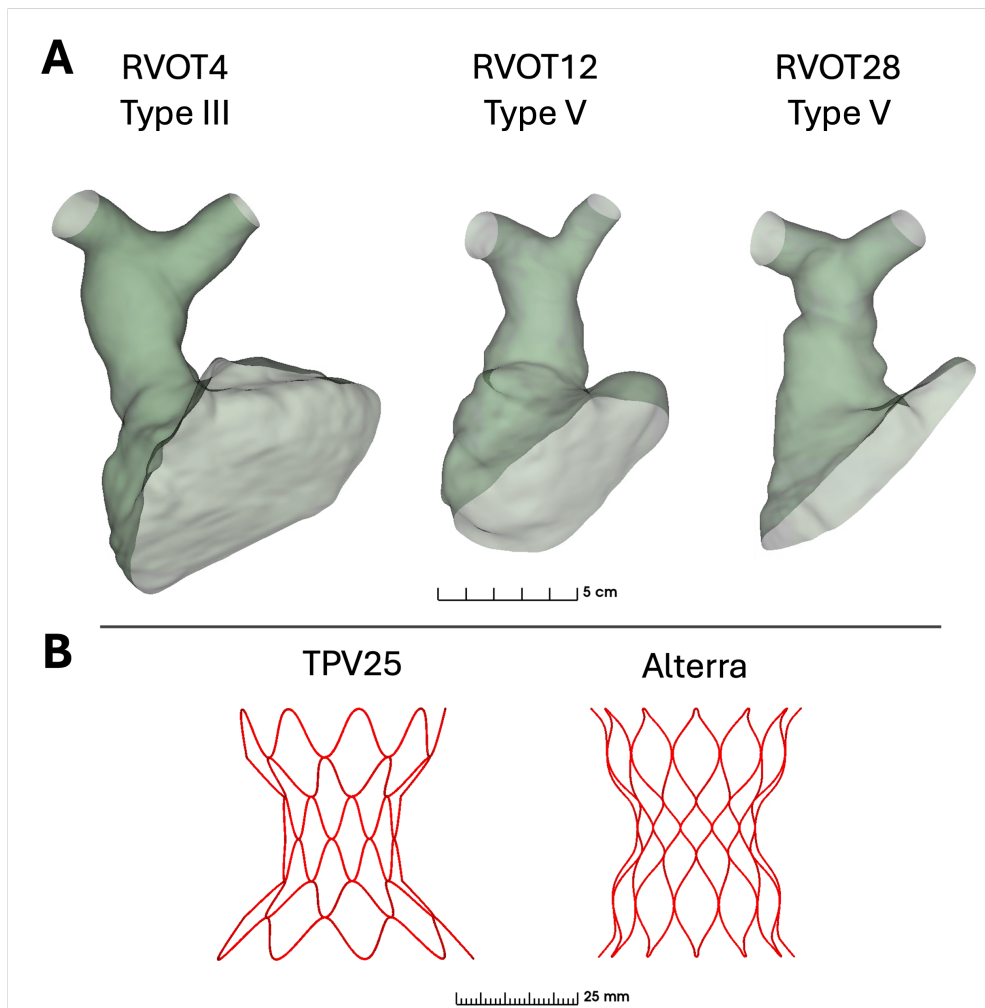
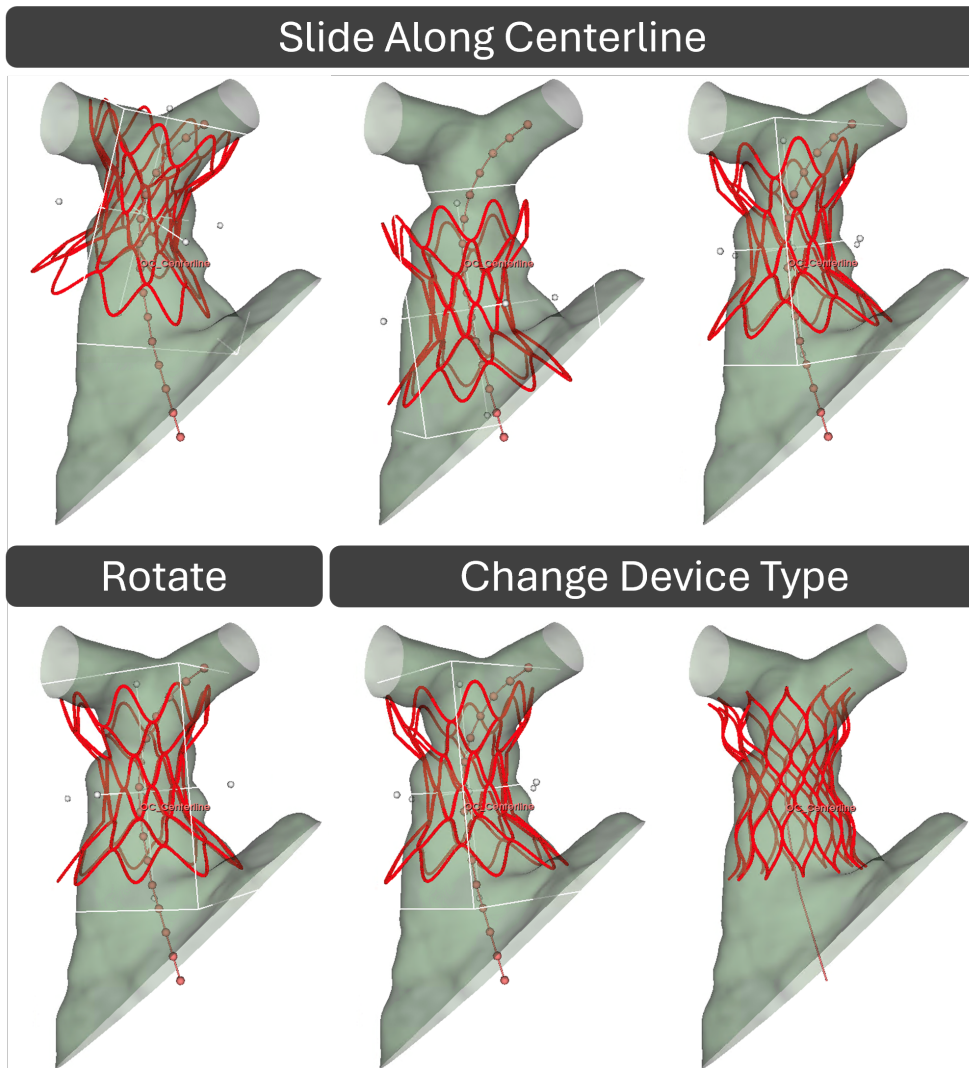


Fig. 1 Overview of Modeling Pipeline



**Fig. 2** A) Shell models of our 3 patient-specific RVOT vessels, to scale. The example vessels were chosen to demonstrate workflow applicability in a range of RVOT sizes and shapes. RVOT morphology types are determined as per [13] B) TPV device models available in the TPVR Simulation module within SlicerHeart.



**Fig. 3** Device placement and TPVR simulation module functionality.

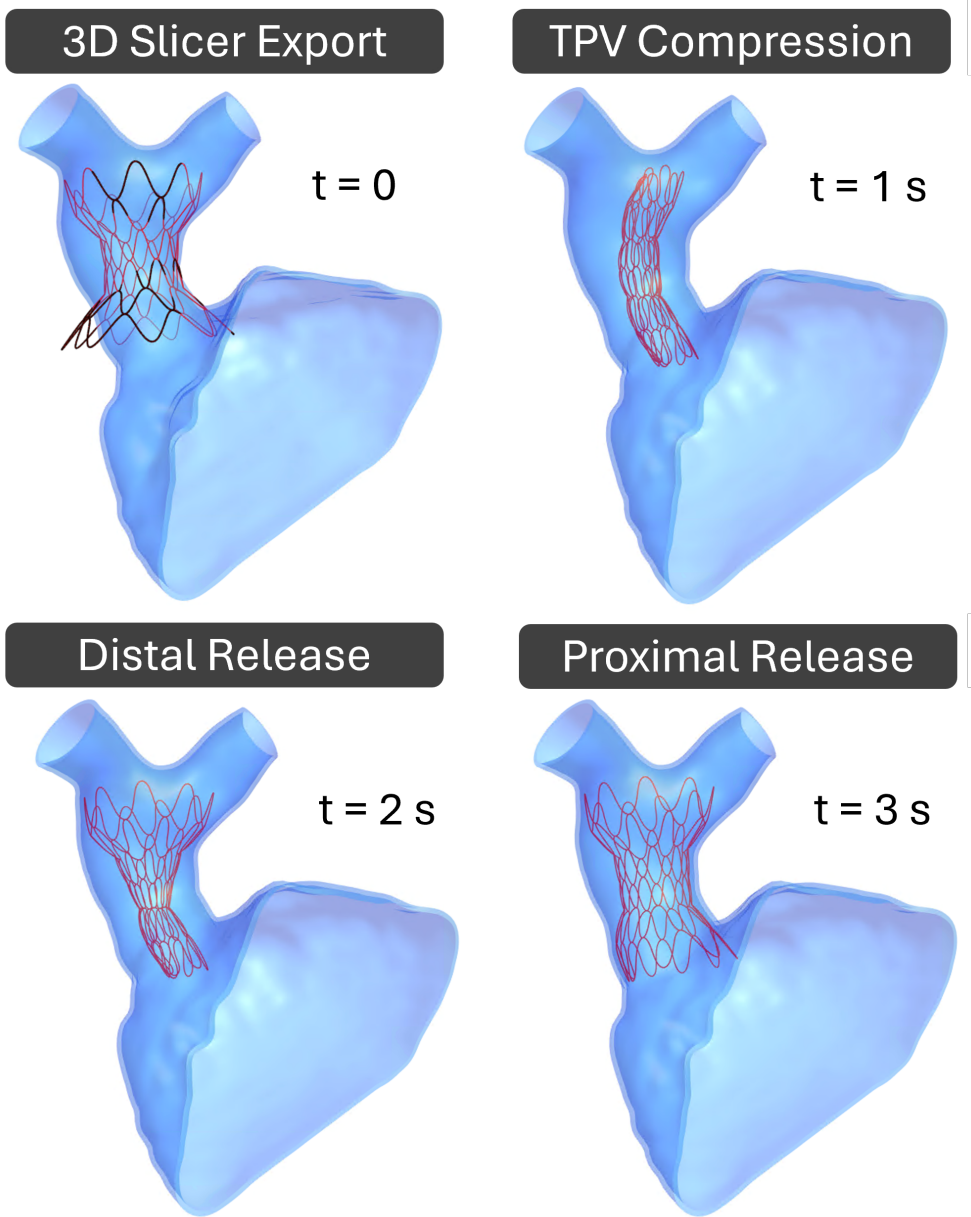
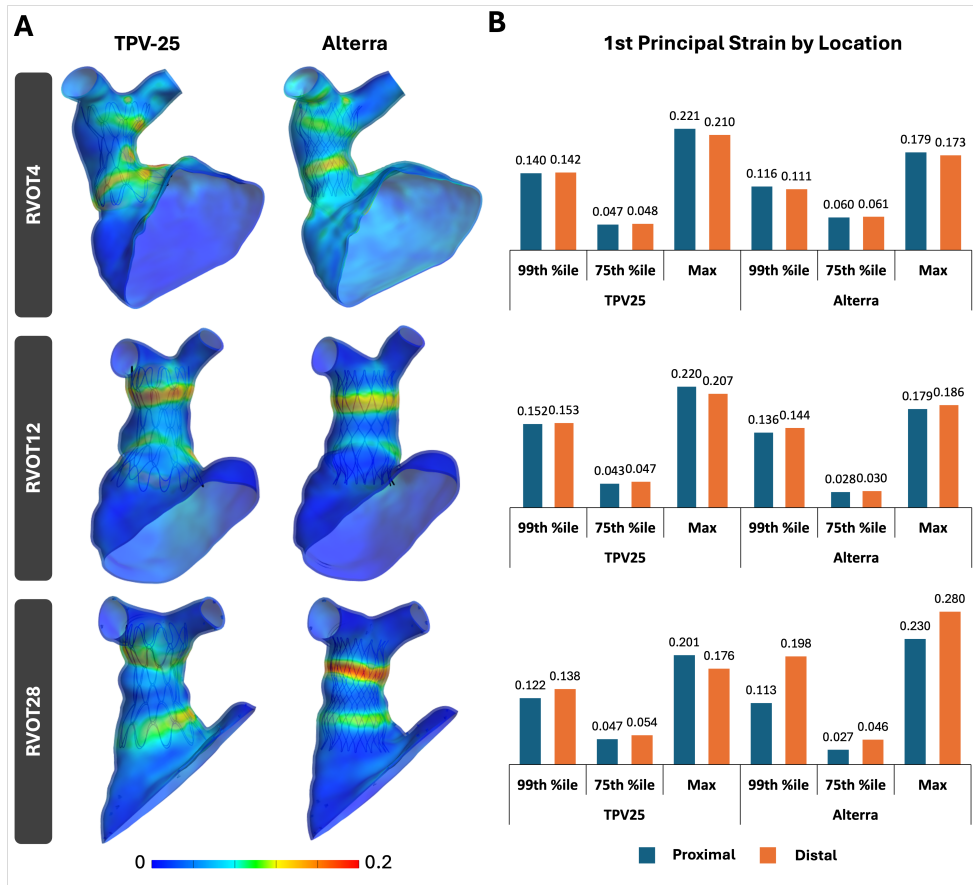
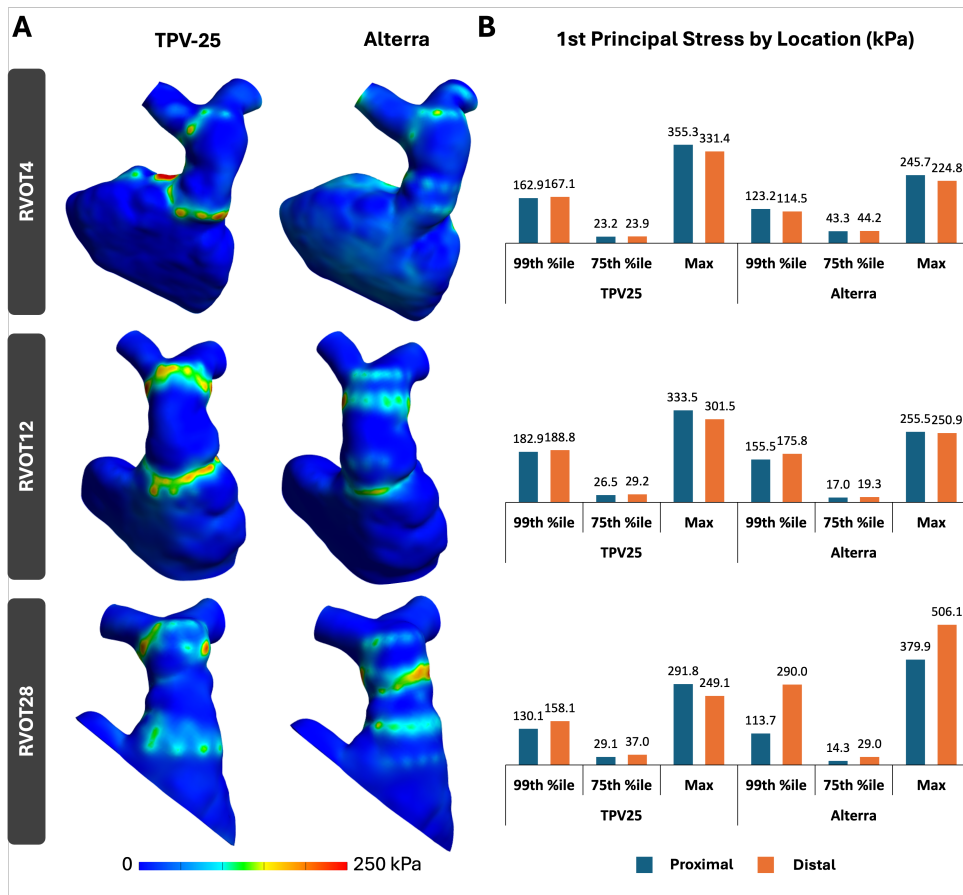


Fig. 4 FEM modeling – staged deployment in FEBio.



**Fig. 5** A) 1st principal Lagrangian strain distribution in simulated RVOT and TPV cases, and B) peak strain values observed in the RVOT across simulated cases, separated by proximal and distal halves.



**Fig. 6** A) 1st principal stress distribution in simulated RVOT and TPV cases, and B) peak stress values observed in the RVOT across simulated cases, separated by proximal and distal halves.

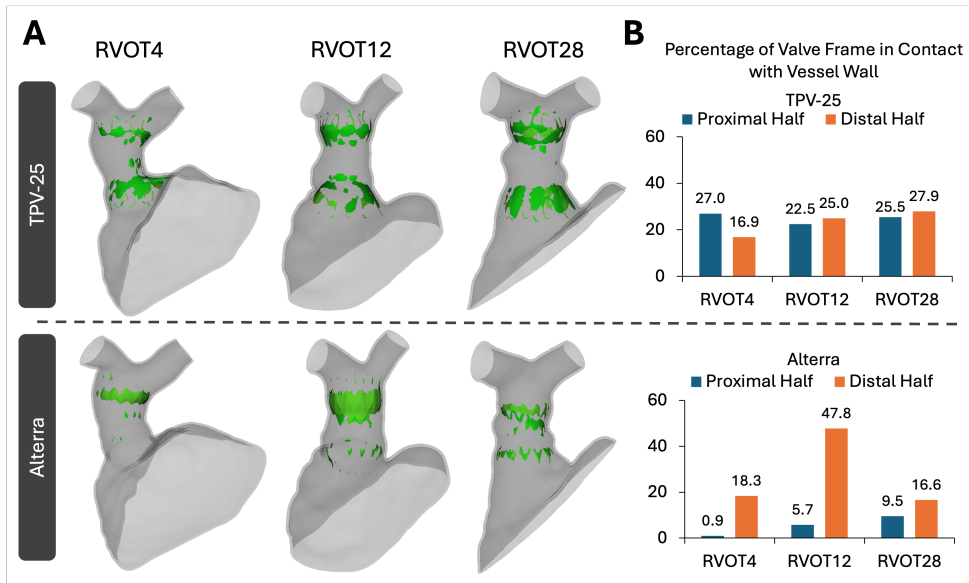


**Fig. 7** Contact visualization for simulated RVOT and TPV cases, A) Visualization of the contact area on RVOT wall across all simulated cases, B) Bar plot depicting the percentage of the stent/valve frame in contact with the vessel wall, separated by proximal and distal halves.